The impact of weathering upon the roughness characteristics of a splay of the active fault system responsible for the massive 2016 seismic sequence of the Central Apennines, Italy

Amerigo Corradetti[1,†], Miller Zambrano[2], Stefano Tavani[3], Emanuele Tondi[2], and Thomas Daniel Seers[1]

[1]*Department of Petroleum Engineering, Texas A&M University at Qatar, Education City, P.O. Box 23874, Doha, Qatar*
[2]*School of Science and Technology, Geology Division, University of Camerino, Via Gentile III da Varano, 62032 Camerino, (MC), Italy*
[3]*DiSTAR, Università di Napoli Federico II, 21 Via vicinale cupa Cintia, 80126 Napoli, Italy*

ABSTRACT

Fault roughness constitutes a key element in the understanding of earthquake nucleation, and surficial asperities on the fault plane play a critical role in slip dynamics and frictional behavior during the seismic cycle. Since it is not generally feasible to recover fault roughness profiles or maps directly at the seismogenic sources, faults at the Earth's surface are typically used as analogues. However, these analogue fault surfaces are often subjected to weathering and erosion, which in turn, reduces their representativeness as seismogenic faults. Rupture along active faults episodically exposes "fresh" fault planes at the Earth's surface, which represent the best available targets for the evaluation of fault roughness generated at seismogenic depths.

Here we present a study conducted on a splay of the Mt. Vettore fault system in the Central Apennines, Italy, along a vertical transect that includes both a weathered and freshly exposed portion of the fault. The latter was exposed after the dramatic Mw 6.5 shock that hit the area on 30 October 2016. We have produced a highly detailed model (i.e., point cloud) of a section of the fault using structure from motion-multiview stereo photogrammetry to assess its roughness parameters (i.e., the Hurst fractal parameter) and to determine the extent to which these parameters are affected by weathering assuming that they had similar fractal characteristics when reaching the surface.

Our results show that weathering can modify the value of the fractal parameters. In particular, by independently analyzing different patches of the fault, we have observed that the smoother and recently exposed portions have an average Hurst exponent of 0.52 while the average Hurst exponent of zones with more prolonged exposure times is 0.64. Accordingly, we conclude that by using high-resolution point clouds, it is possible to recognize patches of faults having a similar intensity of deterioration attributable to weathering.

INTRODUCTION

It has long been recognized that the topographic characteristics of faulted surfaces hold profound implications for the mechanical behavior of the upper crust. Indeed, links between coseismic fault slip and fault surface roughness have been investigated over the past several decades using a combination of numerical, laboratory, and field-based studies (e.g., Brace and Byerlee, 1966; Goodman and Sundaram, 1978; Okubo and Dieterich, 1984; Power et al., 1987; Tullis, 1988; Mora and Place, 1999; Sagy et al., 2007; Bistacchi et al., 2011; Tal et al., 2018). Often a basic prerequisite of such studies is the characterization of asperities upon synthetic or geologic fault surfaces, either in outcrop or within a laboratory setting. Due to limitations in metrological data acquisition, early fault roughness studies were limited to 2D observations (e.g., Brown and Scholz, 1985; Power et al., 1987). More recently, the study of fault roughness experienced renewed interest due to the availability of high-resolution 3D imaging techniques and commensurate increases in the computational power required to process and analyze their output data sets. Concerning field-based studies, the advent of commercially available terrestrial laser scanners (terrestrial LiDAR) provided great impetus for decametric to kilometric fault roughness studies (e.g., Mills and Fotopoulos, 2013; Telling et al., 2017). For lab-based studies, high-accuracy laser profilometers, white light interferometers, and atomic force microscopes have facilitated the investigation of fault asperities from centimeter down to nanometer scales (e.g., Candela et al., 2009; Siman-Tov et al., 2013; Renard et al., 2013; Pluymakers et al., 2017). More recently, structure from motion-multiview stereo (SfM-MVS) photogrammetry has been applied to the characterization of fault roughness (e.g., Corradetti et al., 2017; Olkowicz et al., 2019; Zambrano et al., 2019; Okamoto et al., 2019), which carries the advantage of being highly scalable while only requiring a consumer-grade camera for data acquisition.

The recognition that fault topographies display fractal properties, displaying self-similar or self-affine roughness characteristics across multiple scales of observation, stems from some of the earliest studies on fault roughness (e.g., Andrews, 1980). In particular, it was soon observed that different scaling transformations (i.e., different values of the Hurst exponents) are generally observed both co-aligned with and perpendicular to the fault's slip direction due to fault wearing processes (e.g., Mandelbrot, 1985; Thompson and Brown, 1991; Power and Tullis, 1991; Schmittbuhl et al., 1993). Several methods have been proposed to analyze the statistical properties of fault roughness based on signal processing techniques (e.g., Candela et al., 2009, and references therein). Among these, arguably the most reliable method is by power-law fitting of a Fourier power spectrum $P(k)$ (i.e., the square of the modulus of the Fourier transform: Schuster, 1898) plotted as a function of the wavenumber k in a bi-logarithm scale. Such studies are commonly applied to freshly produced synthetic slip surfaces generated during lab experiments or on natural outcropping fault planes. However, the effect that weathering can have over natural surfaces and hence over their scaling parameters has hitherto never been subject to thorough investigation.

Amerigo Corradetti http://orcid.org/0000-0002-5174-0653

[†]amerigo.corradetti@qatar.tamu.edu.

Indeed, in the case of field-based investigations, previous studies characterizing the roughness of seismogenic faults from outcrop analogues have to assume that fault asperities enjoy almost complete preservation after exposure to weathering. For this reason, freshly exposed parts of active faults represent the most common targets for investigation. Nevertheless, even in optimal cases, the influence of weathering can still be relevant, as testified by those studies aimed to characterize patches of faults having similar exposure times to weathering (Wiatr et al., 2015; Goldberg et al., 2016). For outcrop studies of fault roughness to remain valid, it is necessary to give the role of weathering upon the degradation of fault plane asperities full consideration. Under certain environmental conditions, weathering effects can be particularly relevant in the presence of carbonate rocks whose resistance can also be affected by their thermal history (Pluymakers and Røyne, 2017) or by the presence of mirror-like slickensides coated by nanoscale layers of sintered, low-reactivity phases (e.g., Goldberg et al., 2016).

To assess the influence of weathering over fault roughness parameters of carbonate rocks, we conducted a study on a splay of the Mt. Vettore fault system in the Central Apennines, Italy. The area has been subjected to historical and recent seismicity (Tondi and Cello, 2003), and since the seismic crises of 2016 that exposed several wide, fresh portions of the fault, it has become the focus of numerous studies relating to seismogenic faults (e.g., Smeraglia et al., 2017; Okamoto et al., 2019).

A point cloud of the fault surface was obtained using SfM-MVS photogrammetry. The photo acquisition of the modeled area was performed ~20 days after a major Mw 6.5 earthquake with 315 small (49 cm^2), adjacent sub-portions of the fault analyzed. Both weathered and unweathered sub-portions of the mapped fault have been comparatively analyzed to evaluate the degree to which weathering processes affect the roughness characteristics of faulted outcrop analogues for seismogenic studies. This comparative analysis relies on the idea that weathered patches of the fault had, at their respective times of exhumation, the same roughness characteristics as the recently exposed segments at least within the size of the reconstructed area (involving an along-slip transect of ~2 m). Even though faults evolve with slip (e.g., Brodsky et al., 2011), this condition is plausibly met for well-developed faults in the absence of lithological variations and disregarding local anisotropies (e.g., fractures). Indeed, even though faults with considerable differences in cumulative displacement have in some instances shown an overall smoothing of asperity heights with slip (e.g., Sagy et al., 2007), this smoothing may also imply processes of re-roughening and/or decrease in gouge production with slip (Brodsky et al., 2011), while the presence of fine-grained carbonate nanoparticles can provide lubrication during coseismic slip in well-developed faults (e.g., De Paola et al., 2015).

METHODS

In this study, roughness evaluations were performed using a dense point cloud obtained using SfM-MVS photogrammetry. Amongst the various approaches used for mapping fault surfaces (i.e., LiDAR, laser profilometers, and more recently, SfM-MVS photogrammetry), photogrammetry is better suited to rough terrain conditions (e.g., seismically modified terrain, mountainous areas, or poorly accessible outcrops; Pitts et al., 2017; Corradetti et al., 2018; Giuffrida et al., 2020) since this survey method relies on versatile, low cost, and lightweight equipment (i.e., consumer-grade cameras). The acquisition method followed here has previously been utilized to assess fault roughness down to the sub-millimeter scale (Corradetti et al., 2017). Errors associated with the output reconstructed fault surfaces are conservatively estimated by the authors as being in the order of ~100 μm based upon this previous work.

3D Topography Acquisition via Photogrammetry

SfM-MVS photogrammetry utilizes a series of narrow baseline survey images to estimate camera pose and sparse scene geometry (structure from motion) and generate a dense 3D point cloud-based reconstruction of the mapped scene (multiview stereo). In this study, Agisoft PhotoScan Pro (http://www.agisoft.com) was used to reconstruct exposed patches of the Mt. Vettore fault system. Photogrammetry has several key advantages compared to other approaches employed in field-based studies of fault roughness. Firstly, photogrammetry is a non-destructive method that does not require sampling of the outcrop. Moreover, the method is highly scalable, with the produced vertex spacing related to the distance between the optical center of the camera and the surveyed scene. Thus, photogrammetry can potentially attain higher resolutions than terrestrial LiDAR when correctly employed, and it is able to bridge the gap between terrestrial laser scanning and laboratory-based instruments. Moreover, the resolution of the method could potentially be enhanced by conducting surveys with a macro lens, which would allow extension of the investigated length scales.

Images were taken at different heights, positions, and orientations (with a maximum camera orientation deviation from the normal to the fault plane of 25°) with the aid of a tripod (Fig. 1A). This allowed us to take the images at lower ISOs (sensitivity to light) and higher f/stops (i.e., small apertures and longer acquisition time) than would have been achieved using handheld shooting mode. The adopted acquisition procedure helps to sharpen the background of inclined photographs, increasing the depth of field (Corradetti et al., 2017). The model was constructed using 639 photos that produced a dense point cloud of ~245 million points (Fig. 1B). Since the model was built using non-geotagged photos, the scene was arbitrarily scaled and oriented by the software initially. A scale was included in the scene to enable the scaling factor between the real world and arbitrary reference frame to be ascertained (Fig. 1B). In this work, geo-referencing of the model was irrelevant for the intended analysis (e.g., James and Robson, 2012) and was therefore omitted.
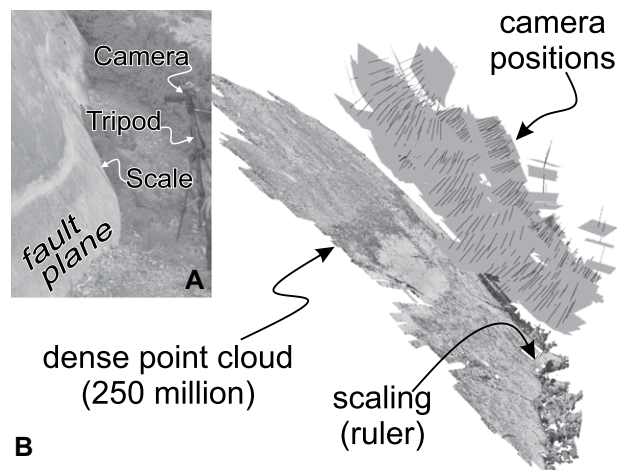

Figure 1. Acquisition workflow is shown. (A) Field equipment consisted of a tripod, a camera, and a ruler for scale. (B) The model was built in Agisoft PhotoScan. The position of the photographs and the scale (between the two circular markers) is indicated. A dense point cloud of ~250 million points was constructed.

Model Pre-processing

The point cloud was trimmed to remove the edges of the model and then cut into 315 regular sub-areas of 49 cm² in alignment with and perpendicularly to the direction of slip. Each sub-area was pre-processed in MATLAB to facilitate resampling into regularly spaced grids. The code used was modified from Corradetti et al. (2017). Each sub-area was loaded into MATLAB as an xy matrix containing fault asperity heights and re-oriented independently to align the direction of the normal to the best-fit plane to the roughness dimension (Fig. 2A). This step was necessary since the mapped fault plane is slightly undulated, which creates localized deviations in orientation with respect to the fault surface. Subsequent to the aforementioned transformation, the residual distances (i.e., the error) from a best-fit plane of the fault patch vertex-set and its corresponding asperity heights are obtained (Figs. 2A–2B). Finally, linear interpolation of the fault patch's unordered point set is used to create a regularly sampled grid of the surface, whereby the grid spacing was chosen to match the average distance of points of each segmented fault patch.

For each sub-area, the output of this point cloud processing procedure is a matrix containing regularly sampled fault surficial asperities (Fig. 2C).

Roughness Evaluation

Fault roughness of each sub-area was characterized by the standard deviation of the residual distances from its plane of best fit and by an evaluation of self-affinity using a Fourier Power Spectral Density (PSD) approach. The latter provides an objective description of the roughness based on the distribution of the amplitudes and wavelengths of the asperities (Brodsky et al., 2011; Candela et al., 2012; Bistacchi et al., 2011). In essence, the PSD as a function of the wavenumber (k) in a bi-logarithmic scale graph of a self-affine function exhibits an apparent linear slope, which is defined from the following power law

$$P(k) = \alpha \cdot k^{-\beta} \qquad (1)$$

where α is the pre-factor and the β is the exponent of the power law. The latter parameter (β) is related to the scaling exponent or Hurst exponent (H) along the direction of the analyzed signal through:

$$H = (\beta - 1)/2 \qquad (2)$$

The self-affinity of a fault is thus defined by the ratio of the Hurst exponent and of the pre-factor calculated perpendicular and parallel to slip (i.e., H_{perp}/H_{slip} and $\alpha_{perp}/\alpha_{slip}$).

Standard Deviation of Singular Value Decomposition Residuals

Standard deviation is one of the most commonly used metrics to describe deviation from the plane of best fit (i.e., residual distances). Several methods exist for the fitting of least square planes through vertex data, such as planar regression (e.g., Fernández, 2005), orthogonal regression (e.g., Jones et al., 2016), and moment of inertia analysis (i.e., principle component analysis of PCA: e.g., Seers and Hodgetts, 2016). In this work, we have calculated residuals using singular value decomposition (SVD) (e.g., Golub and Reinsch, 1971), which is readily executable in high-level programming languages such as Matlab, R, Octave, and Python (i.e., via the NumPy library). SVD is a matrix decomposition method widely used to solve regressions of independent variables (or principal components) returning the direction of the vector, which minimizes the residual variance (smallest singular value). Through SVD, the original matrix (i.e., each of our sub-areas) is factorized as the product of three

A

B PhotoScan PC

C Matlab PC (Rotated and resampled)

- Data centroid
- Best-fit plane in Photoscan coordinates
- Normal to best fit plane
- Point with positive residual
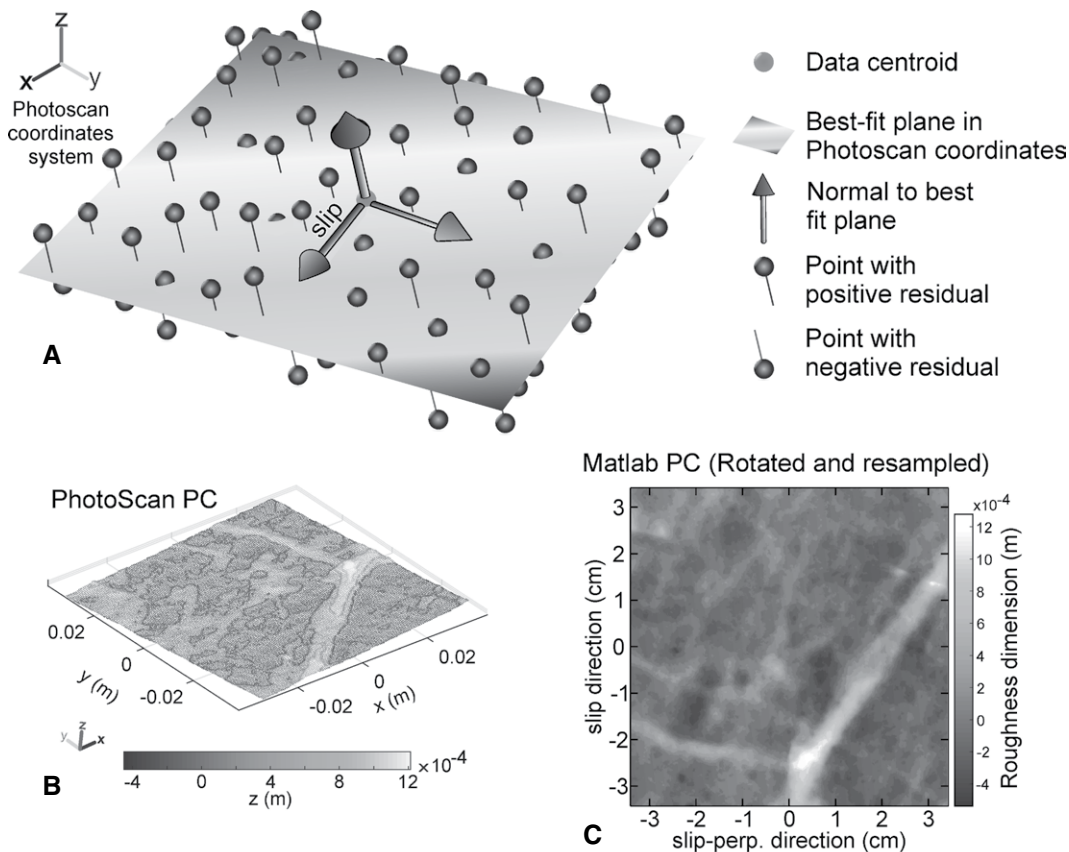- Point with negative residual

Figure 2. Change of base and resampling workflow are shown. (A) A best-fit plane is calculated through singular value decomposition. The origin of the new coordinate system is placed in the centroid of the point set. The z-axis is aligned with the direction of the residuals while the other two axes are aligned parallel and perpendicular to the direction of slip. (B) One of the clouds prior to rotation (i.e., with arbitrary location and orientation). (C) Rotated and resampled point cloud with z aligned to the normal of the fault surface's plane of best fit.

3

matrices, namely U, S, and V. S is a diagonal matrix whose diagonal entries are the singular values. The index position of the minimum value of the diagonal elements of the matrix S is used to identify the column in U, where the normal distances to the best-fit are stored and multiplied for the smallest singular value in S, which also represents the scaling transformation of the SVD. This returns a vector containing all the residual distances of the smallest singular value (i.e., all the perpendicular distances of each point to the plane of best-fit). V contains the directional cosines of the three singular values, which are used to re-orient the sub-areas as described in the previous section.

Fourier Power Spectral Density Analysis

The fast Fourier transform (FFT) analysis of each resampled surface was achieved using a 1D FFT approach (e.g., Renard et al., 2013). Each topographic profile was extracted from the regularly sampled point cloud along a specific direction (i.e., corresponding to transects parallel and perpendicular to the fault's slip direction). Then each signal was analyzed independently (Fig. 3A). The sampling rate (or spatial frequency) was set twice the sampling interval of the vertex cloud in order to omit the highest frequencies. This rules out any potential influence of the acquisition protocol to the results of the roughness analysis. A Hann windowing (Fig. 3B: black line) was introduced to the signal to reduce the amplitude of the discontinuities at the boundaries and emphasize the characterization of each sub-cloud at its center. The FFT function was thus performed on the windowed signal (solid black line in Fig. 3A). The result is a spectrum that is symmetric around its 0-frequency component (i.e., Nyquist component or
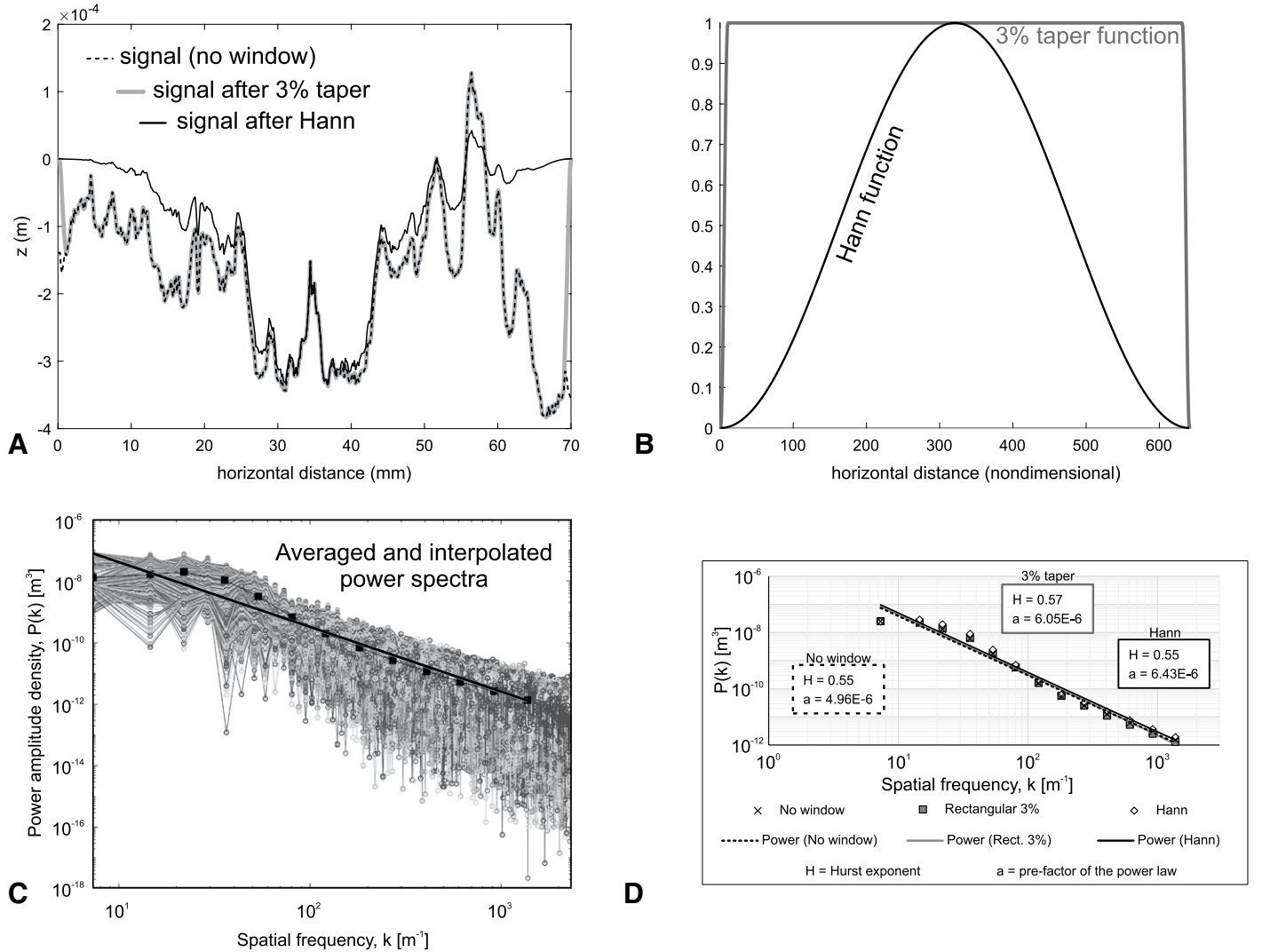

Figure 3. Fast Fourier transform method is shown. (A) A signal is extracted from the surface and (B) a Hann windowing is applied. The effect of a 3% taper function is also shown for comparison. The Hann windowing was chosen to focus the analysis of the signal in its central zone and avoid boundary effects. (C) Fourier power spectra of several profiles calculated along the direction of slip of the sub-area shown in Figure 2C and plotted in a k vs. P(k) log-log plot. Profiles were then averaged using regularly spaced log(k) intervals. (D) A plot of the results of three power spectra calculated using an un-windowed signal, a 3% taper function windowing, and a Hann function windowing. In the presented case, which refers also to the surface displayed in Figure 9C, the Hann windowing shows a Hurst exponent similar to the un-windowed case, while the rectangular 3% taper windowing is closer in terms of pre-factor. The break of slope seen in these power spectra is caused by the presence of a "deep" (~1 mm) incision in the surface.

mean of the signal). Therefore, half of the resulting spectrum was trimmed of its redundant negative component and the signal was multiplied by two to keep the same energy but disregarding for the Nyquist odd component, which is unique if present. A Hann Amplitude Correction Factor (ACF) of two was selected to recover the loss of signal "energy" due to the selected windowing. The Fourier power spectrum P(k) was thus calculated as the square of the modulus of the Fourier transform (Schuster, 1898; Fig. 3C).

All power spectra associated with each direction (i.e., parallel or perpendicular to slip) were stacked and averaged in a geometric progression with a regularly spaced frequency (k) (Fig. 3C). Averaging in geometric progression allowed the computation of the best fit of the form of Equation 1 that is not biased by a differential in the frequency of shorter and longer wavelengths.

The selected resampling method, the windowing with related corrections (Fig. 3D), as well as the choice of the spacing for the averaged geometric progression of the power spectra can directly affect the best fit coefficients, especially when observations are made through

limited scale orders. For this reason, all of the 315 subsampled fault surfaces were analyzed using the same procedure on patches of the same size characterized by comparable point densities. In Figure 3D, however, the effect of using null windowing and a 3% taper function windowing (e.g., Candela et al., 2012; Bistacchi et al., 2011) over Hann windowing applied in this study is also shown. As per the example shown, the results are not really affected by the chosen windowing.

DATA

In this section, the geological framework of the study area, field observations, and specific segments of the analyzed fault system are presented.

Geological Framework

The studied fault is located within the Northern Apennines of Central Italy (Fig. 4). This area has experienced recent and historical seismicity related to the transtensional collapse of

the Northern Apennines orogenic system (e.g., Mazzoli et al., 2005; Porreca et al., 2020). In this study we focused on the Mt. Vettore-Castelluccio di Norcia area, which was struck during a seismic crisis in 2016. The seismic sequence comprised three mainshocks: (1) Amatrice, Mw 6.0 on 24 August; (2) Visso, Mw 5.9 on 26 October, and (3) Norcia, the most powerful earthquake of the sequence at Mw 6.5, on 30 October 2016 (e.g., Chiaraluce et al., 2017).

The surface rupture caused by this seismic sequence has been well documented by the Open EMERGEO Working Group (Civico et al., 2018; Villani et al., 2018). These authors reported that the coseismic ruptures are generally organized in a systematic pattern of dominantly synthetic (N135°–160° striking, SW-dipping) and subordinately antithetic (N320°–345° striking, NE-dipping) components. In most of the cases, the ground ruptures follow the trace of mapped faults (e.g., Pierantoni et al., 2013, and references therein) and sometimes are located along fault splays that were not previously mapped (Civico et al., 2018). The average coseismic throw of the entire sequence is ~0.3 m. However, more
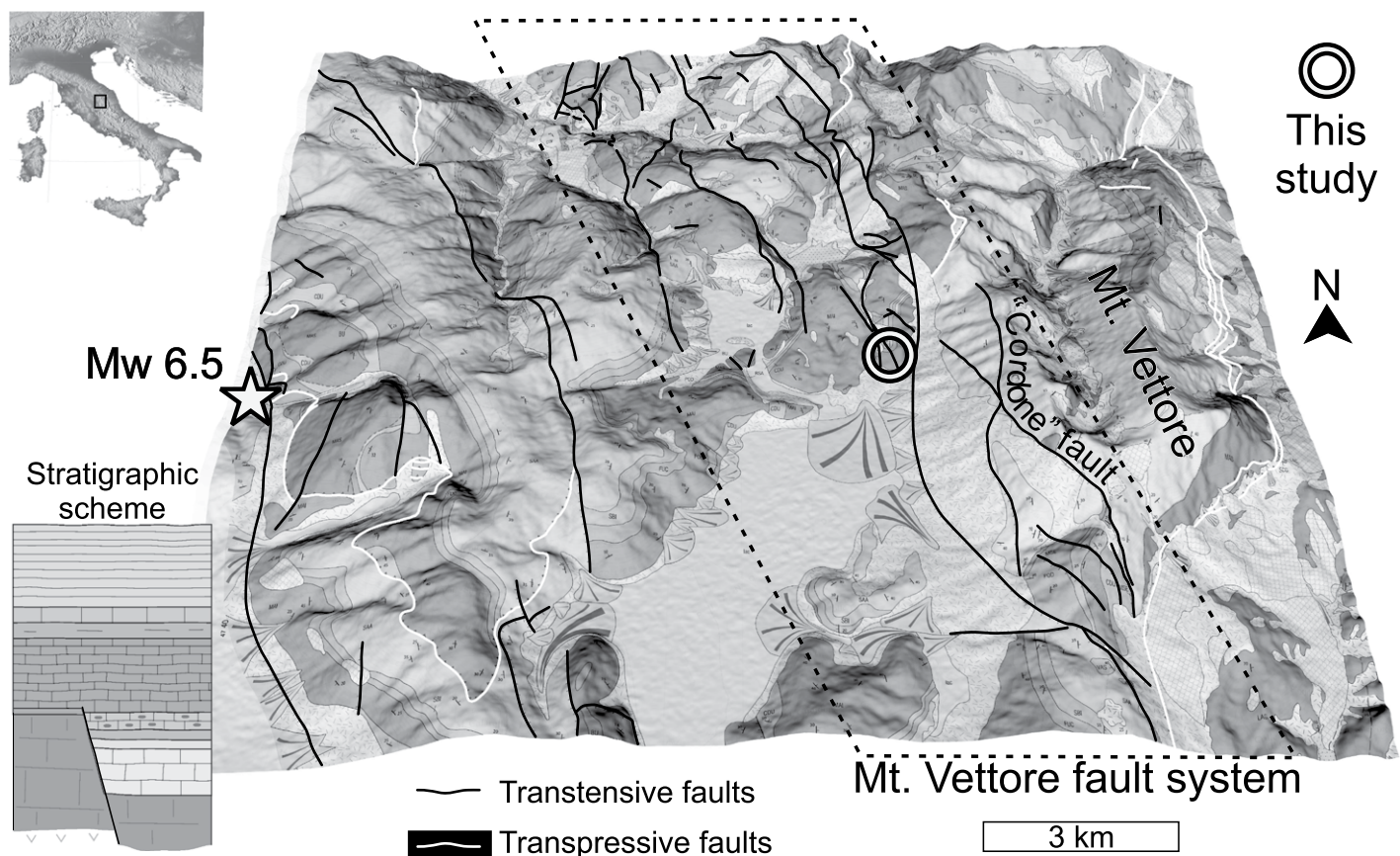

Figure 4. Map shows geological framework of the area modified from Pierantoni et al. (2013) and draped over the ASTER Global Digital Elevation Model NetCDF V003 (NASA/METI/AIST/Japan Spacesystems and U.S./Japan ASTER Science Team, 2019). The splay studied is part of the Mt. Vettore fault system. A star indicates the epicentral location of the Mw 6.5 event described in the text.

than 2 km of the ruptures were characterized by an average coseismic throw higher than 1 m, with maxima of near 2.5 m along the so-called "Cordone del Vettore" or the Mt. Vettore fault scarp (Civico et al., 2018; Villani et al., 2018). Prior to the 2016 seismic crisis, many of those faults belonging to the Mt. Vettore fault system were classified as "dormant" faults (Galli and Galadini, 1999), a term used to indicate faults that show geological evidence of Holocene (<0.0117 m.y.) surface ruptures, which are not associated with historical earthquakes.

The component of the Mt. Vettore fault system analyzed in this study represents a splay within the vicinity of Colli Alti e Bassi (Figs. 4 and 5). In this locality the Mesozoic carbonate basinal sequence is downthrown by a NNW–SSE-striking normal fault exposing the slickenside of the footwall block. In this study area the overall newly exposed displacement is around 1 m. It is challenging to assess if this represents the sole contribution of the fault displacement or if this was partly enhanced by compaction of the deposit bracketing the fault above the hanging wall block during coseismic shaking.

Fault Morphology

The outcrop studied is situated ~1.4 km above sea level, meaning that it is affected by seasonal cryoclastism (i.e., enhanced weathering and erosion due to freeze-thaw cycles inside fractures). The topography of the fault is also affected by erosive hydraulic action due to surface runoff down the fault scarp (Fig. 5). The latter alteration mechanism results in erosional artifacts that overprint seismogenic fault plane asperities caused by shearing and abrasion at an angle of ~21°. This angle is hence the combined result of the paleo-slip recorded on this fault surface with

respect to its geodetic nadir (i.e., the direction of surface runoff), and it is strictly related to the pitch angle of the fault (i.e., the angle between the strike of the normal fault and the slip vector) (Figs. 5 and 6A).

Four zones were distinguished in the field and in the resultant outcrop model (Figs. 5 and 6A), which we have ordered from the bottom of the section to the top. Zones 1 and 2 show a whitish colored cataclastic slickenside. Notably, Zone 1 was only exhumed during the Mw 6.5 earthquake of 30 October 2016. This was only ~20 days prior to image acquisition. Preceding this earthquake, this surface was in contact with the earthy Quaternary deposit bracketing the fault as often observed along basin bounding normal faults (e.g., Collettini et al., 2003; Agosta and Aydin, 2006). At the time of photo acquisition, this zone was hence contaminated with soil and thus unsuited for seismogenic evaluation. Zone 2 was exposed earlier during the same seismic sequence. The smooth cataclastic slickenside is preserved as small patches within Zone 3, while extended exposure to weathering (likely >1.5 ka; e.g., Galli et al., 2019) has completely removed it from Zone 4. The exhumation of Zone 3 began with the first major event of the 2016 seismic crises on 24 August. These zones do not exhibit uniform height along the fault (Fig. 5). A few decimeters northward from the modeled area, Zones 2 and 3 are either shallower than on the eastern side of the model or not present at all (see Fig. 5).

The analyzed fault topography is also affected by fracturing, which is particularly intense in the present study area. Many of these fractures are associated with their slip direction as they are oriented at a high angle (~90°) with respect to it (e.g., Doblas, 1998). Due to the altitude of the analyzed fault, the apertures of the observed

fracture array tend to show enhancement by cryoclastism.

The sub-areas of the fault model were extracted parallel and perpendicular to the main slip direction (Fig. 6B). Manifest as a long wavelength undulation, the main direction of slip was made evident after calculating the fault distance from a best-fit plane (Fig. 6B). The 315 analyzed point clouds are squares with sides of 7 cm (Fig. 6C). The average point density for each sub-region is 92 ± 8 points per mm^2, which corresponds to an average spacing of ~0.1 mm.

RESULTS

The results presented here are based on the division of the fault model into four areas (Fig. 7A). This division is based upon anecdotal observations pertaining to the macroscopic preservation of cataclastic slickensides as detailed above. The normalized frequency distribution of the standard deviation of the residuals is plotted in bins of 0.2 mm (Fig. 7B). Twenty-seven percent of the sub-models of Zone 2 (the "unaltered" slickenside zone) display a standard deviation below 0.2 mm. Fifteen percent of Zone 1 is represented in this bin. Notably, only 3% of the sub-models of Zones 3 and 4 are represented overall in this bin. Dashed lines in Figure 7B represent the normal distributions over 1000 randomly generated numbers using the mean and standard deviation of each population of individual bins after trimming the maxima and minima (n = 3). With the aid of this visual tool, it is clear that Zone 2 exhibits the highest degree of smoothness, in terms of asperity heights evaluated via standard deviation, and the lowest variance.

Since pervasively fractured regions influence the roughness of the fault in an unpredictable, non-time-dependent manner, we removed all sub-models that have high densities of large open fractures, which were identified using the red, green, and blue channel of the outcrop model (Fig. 6A). The areas removed are highlighted in red in Figure 7A. This selection was purely qualitative. As shown in the normalized frequency distribution after this filtering (Fig. 7C), most of the roughest sub-models were excluded. Indeed, all sub-models with standard deviations of residuals larger than 1.2 mm were omitted from the data set through the selective removal of ostensibly fractured areas of the outcrop (Fig. 7C). By removing the roughest sub-models, which would have otherwise skewed the analysis, the frequency distributions of the four populations acquire more distinctive distributions than prior to trimming.

A more optimal way to visualize the distribution of the standard deviation of residuals
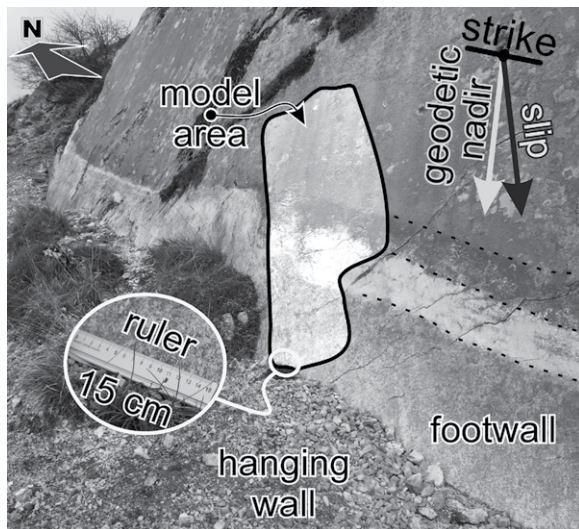

Figure 5. Photograph shows the fault studied with the location of the reconstructed model and the ruler used for scaling the model (42°50′10.02″N, 13°13′46.3″E). The footwall block is characterized by four zones separated by three dashed lines. The directions of the wear striations (i.e., slip direction) and the slope (surface runoff-driven erosion) are also indicated.
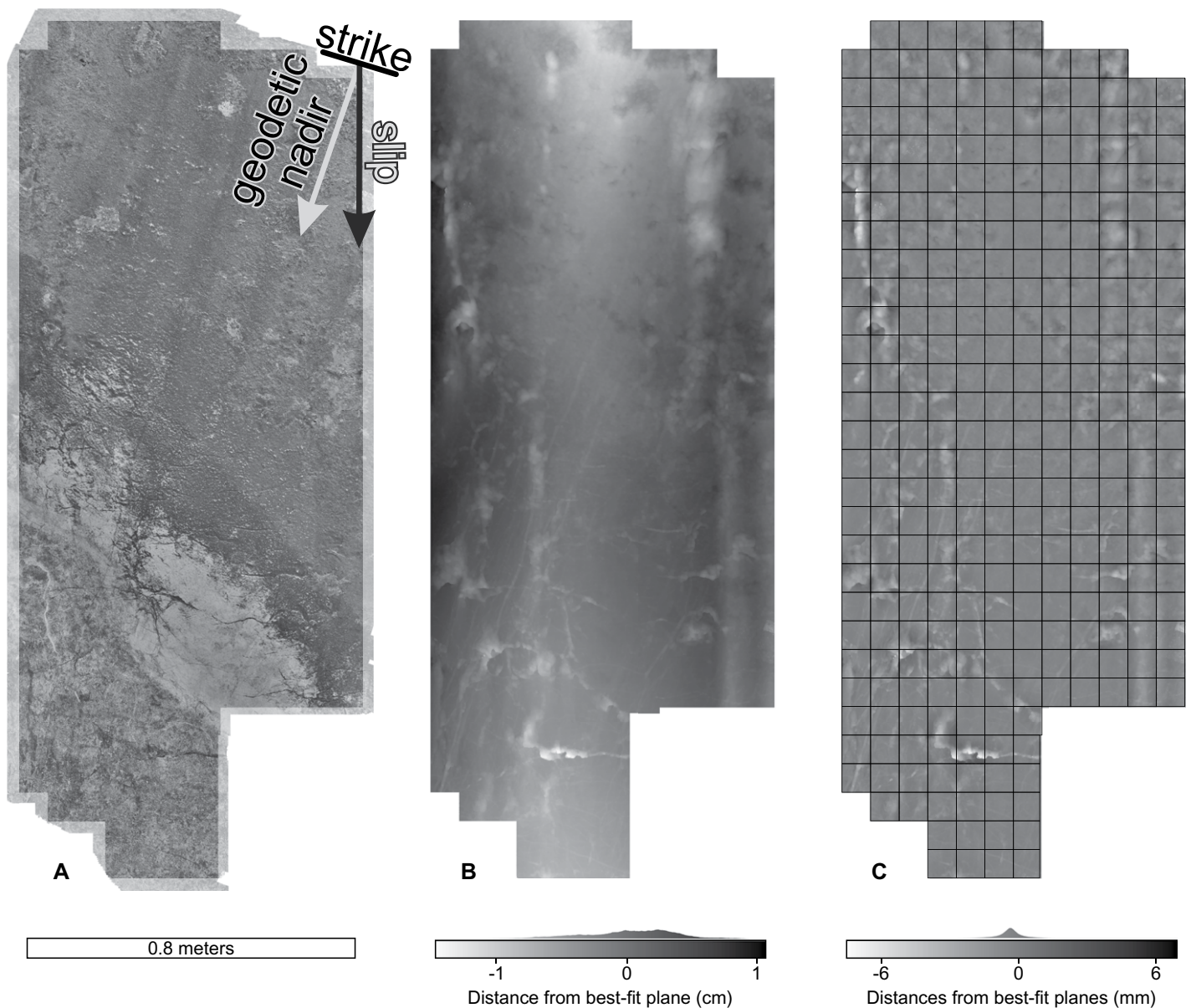
Figure 6. The model analyzed is shown. (A) View of the model extracted from PhotoScan. (B) The distance of the point cloud from a plane of best fit with distance distribution (calculated in CloudCompare). (C) The distance of each sub-sampled point cloud from its respective plane of best fit.

for each sub-model is to plot their cumulative distribution (Figs. 7D–7E). In both the complete data set and filtered data set, the cumulative distribution shows clear scaling relationships. Deviations from the parametric form may also be the result of distinctive sub-zones that were erroneously subdivided during definition of the four major sub-regions of the outcrop model; for instance, Zone 4 may have been exposed by multiple surface ruptures or by compaction of the debris material lying on top of the hanging wall block triggered by one of several historical earthquakes that hit the area without breaking to surface (Galli et al., 2019).

Having established that open fractures constitute noise within the time-dependent weathering of the fault topography by enhancing the roughness signature of the fault surface studied, the core component of the roughness analysis was conducted using fault patches filtered for the presence of major discontinuities. The normalized frequency distributions of Hurst exponents along the two directions exhibit similar behavior (Figs. 8A–8B). Zone 2 is characterized by a narrow distribution with more than 60% of the populations within 0.44 and 0.59 for both slip parallel and perpendicular transects. Zone 3 also presents narrow distributions at slightly higher values

with more than 70% of the population within 0.54 and 0.69 for both directions (Figs. 8A–8B). Zones 1 and 4 present wider distributions (i.e., relatively high standard deviations) with means higher than those of Zones 2 and 3. Averaged Hurst exponent values for Zones 1 and 4 are 0.58 and 0.64, respectively. The frequency distributions of the pre-factor of the power-law show similar clustering (Figs. 8C–8D). For Zone 2, ~90% and 74% of the measured population is smaller than 1×10^{-5} parallel and perpendicular to the slip direction respectively (Figs. 8C–8D). Zone 4 is characterized by wide variability in the pre-factor populations. Comparable with
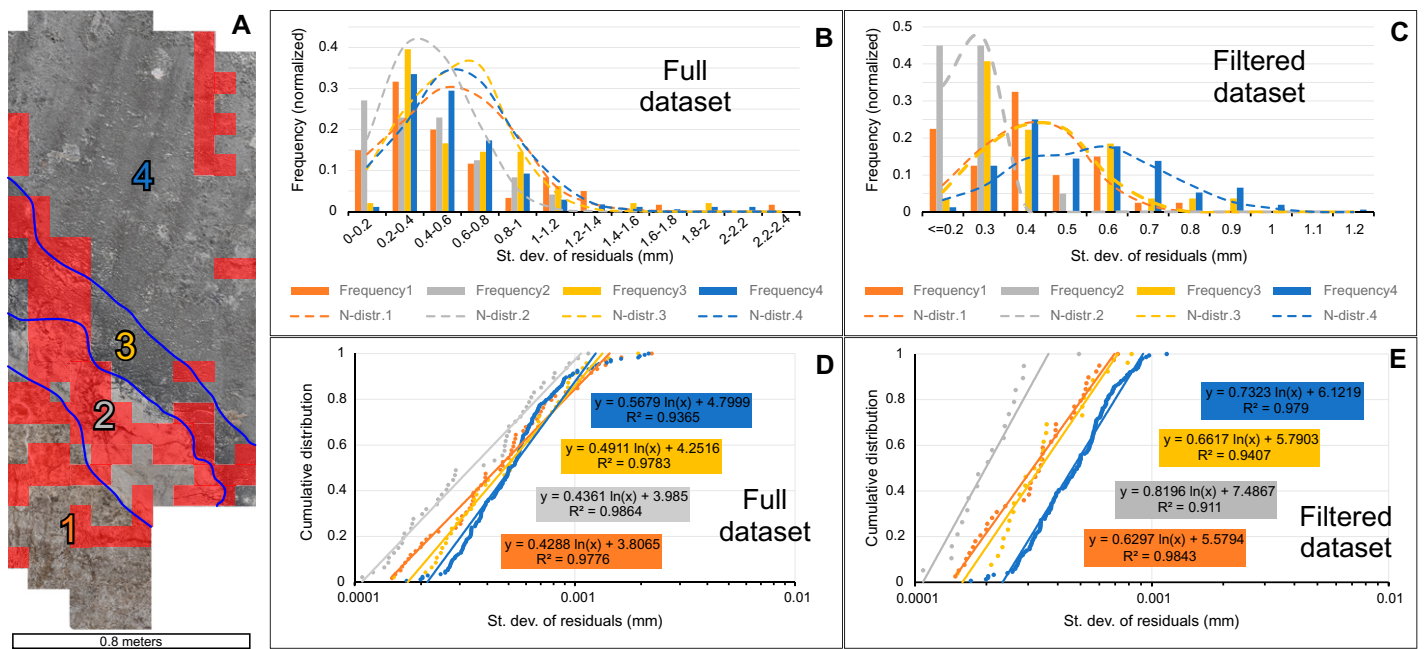
Figure 7. Analysis of the standard deviation (st. dev.) of the singular value decomposition residuals is shown. (A) Fault surface showing the division in four different zones and the part of the fault most heavily carved by fractures. (B) Normalized frequency distribution histogram of the standard deviation of the residuals for all 315 sub-models plotted in bins of 0.2 mm each. (C) Normalized frequency distribution histogram of the standard deviation filtered of the red zones indicated. (D) Cumulative distribution of the standard deviation of residuals displayed semi-logarithmically prior to and subsequent to (E) filtering. Dashed lines are 1000 values that were randomly generated using the mean and the standard deviation of each population described above.

observations pertaining to the distribution of standard deviation, Zones 2 and 4 represent two end-members in the frequency distribution of Hurst exponents and pre-factors. The self-affinity of the analyzed sub-models is represented by their Hurst exponent ratios (H_{perp}/H_{slip}) and by their pre-factor ratios (a_{perp}/a_{slip}). The frequency distribution of both H_{perp}/H_{slip} and a_{perp}/a_{slip} for Zone 2 (Figs. 8E–8F) is clustered around 1, while a slightly higher clustering rate (<1.05) is observed for Zones 1, 3, and 4.

DISCUSSION

In this work we have used digital photogrammetry to estimate the roughness of fault zones exposed to subaerial conditions over different timescales. To assess the extent to which exposure time impacts asperities generated during fault rupture (e.g., Wei et al., 2013), we used several quantitative roughness indicators calculated directly using the reconstructed fault surface. To quantify the roughness with respect to asperity heights, we used the standard deviation of the residual distances between the faulted surface and plane of best fit as calculated using SVD of the reconstructed fault surface's point set. We also assessed roughness through the computation of the PSD of the FFT to quantify the roughness in terms of spatial frequency. We then esti-

mated the Hurst exponents and pre-factors of the scaling transformation both parallel to and perpendicular to the direction of slip. The standard deviation of the residuals indicates a clear and somewhat expected relationship between exposure time and roughness (Fig. 6). The exponents and pre-factors of the scaling transformation also indicate that zones of the analyzed fault surface have been altered by weathering processes (Figs. 8A–8D). In this regard, higher Hurst exponents and pre-factors are found for those areas of the fault exposed for a longer duration, with Zones 2 and 4 of the fault representing two end-members (Fig. 7A). The relation between the alteration intensity and anisotropy of the scaling transformation is less evident (Figs. 8E–8F) but present. Previous studies on natural faults have documented self-affine behavior with two distinct scaling transformations along the direction of slip and perpendicularly to it (Mandelbrot, 1985; Power and Tullis, 1991; Schmittbuhl et al., 1993; Candela et al., 2009). This self-affinity has been more recently quantified over several length scales, with an overall H_{perp}/H_{slip} ratio of ~1.33 (e.g., Candela et al., 2012; Renard et al., 2013), which terminates at the micrometer-scale where a transition to an isotropic scaling roughness occurs (Siman-Tov et al., 2013; Candela and Brodsky, 2016; Okamoto et al., 2019). The fault studied in this work is, however, quite isotropic

in origin as shown by the clustering around 1 of both H_{perp}/H_{slip} and a_{perp}/a_{slip} for Zone 2, which is the least weathered and most recently uncovered zone. This latter zone is mostly characterized by undulations with wavelengths larger than the analyzed sub-model's size (Fig. 6B) and exhibits indistinct striations (Fig. 6C). The result is that at our scale of observation (i.e., power spectra spatial frequencies within 0.2 mm^{-1} to 7 cm^{-1}), weathering contributes to building anisotropy more than the inherited wear (Figs. 6C and 8E–8F). Hurst exponents and pre-factors are strictly correlated, with the Hurst exponent dependent from the slope of the interpolation (Equation 1–2) and the pre-factor being the vertical intercept (Equation 1). Accordingly, it is not surprising to observe similar behavior between H_{perp}/H_{slip} and a_{perp}/a_{slip} for a given zone. This aforementioned along-gravity imprinting is not truly aligned to the faults' slip vector, with the fault also being characterized by a minor strike-slip component in a moderately oblique direction of ~21° to the direction of slip. It is worth noting that if this angle were lower, the effect of weathering could be easily misinterpreted as slip grooves.

Examples of physical processes that may be contributing to telogenetic alteration of the fault are the action of the impact of water drops or hail against the surface, erosion due to surface runoff, and physical disintegration of the fault
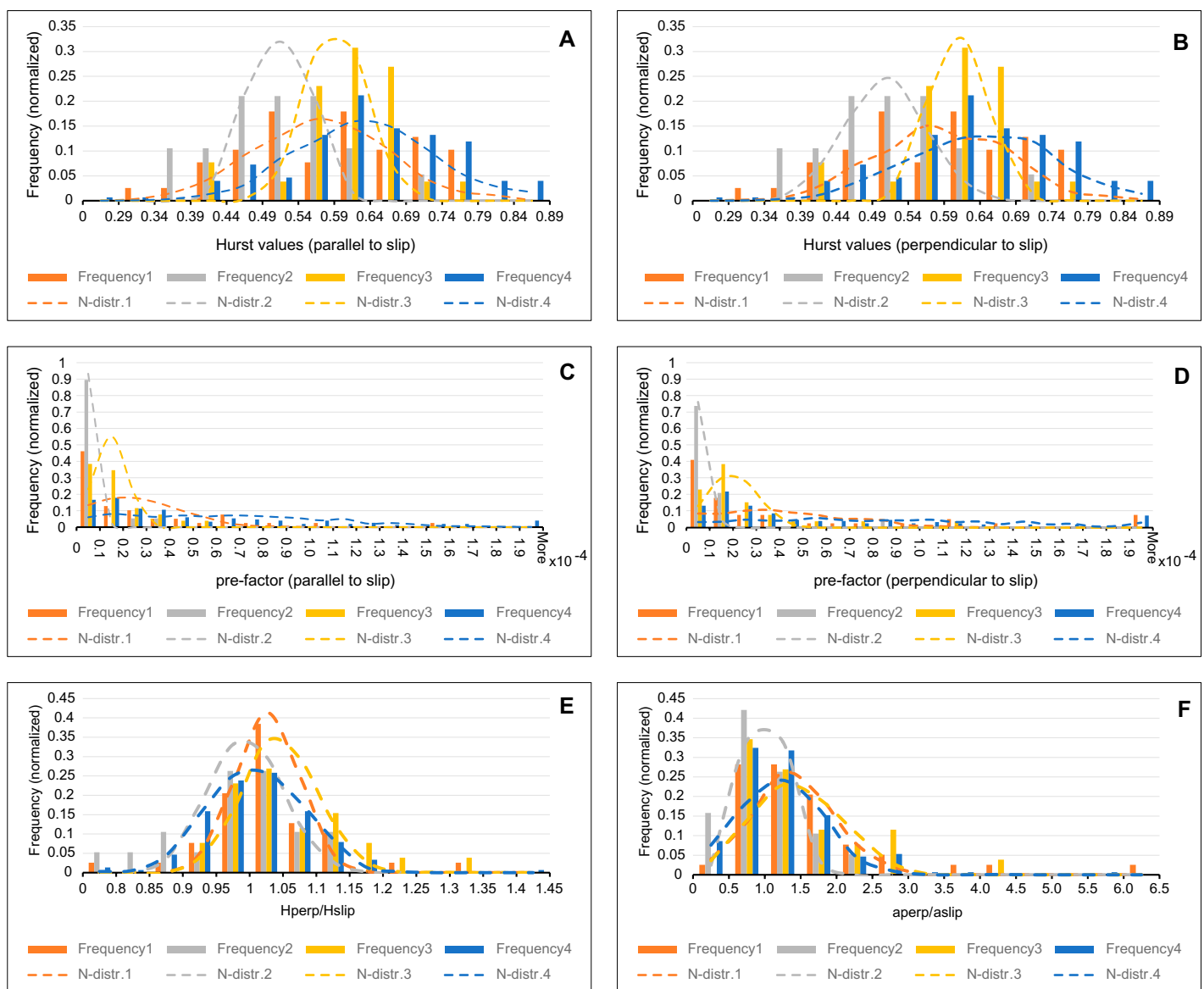
Figure 8. Results of the fast Fourier transform analysis are shown. Normalized frequency distributions of the Hurst exponents along (A) the direction of slip and (B) perpendicular to slip. Normalized frequency distributions of the pre-factor (C) along the direction of slip and (D) perpendicular to slip. Frequency distribution of (E) the Hurst exponents and (F) pre-factors ratio calculated between the perpendicular to slip direction over those aligned to the slip direction. Dashed lines represent the normal distributions over 1000 randomly generated numbers using the mean and the standard deviation of each population described above.

plane by freeze-thaw action. In addition to physical weathering, dissolution and precipitation of the carbonate host rock via contact with meteoric water is likely to be a significant weathering agent that contributes to the fault plane alteration. Chemical reactions operate at the scale of the minerals, breaking down their chemical bonds.

The depletion of roughness representative of seismogenic conditions with increasing exposure time is clearly visible in Figure 9, where three sub-regions are shown. These represent, from left to right, a sub-region from Zone 4 (roughest) with the closest standard deviation to the average for the entire Zone 4 (Fig. 9A), a sub-region from Zone 2 (smoothest) with the smallest standard deviation (Fig. 9B), and a sub-region from Zone 2 with the average standard deviation for Zone 2 (Fig. 9C). Their power spectra along slip and perpendicularly to slip indicate that the smoothest surface has the smallest Hurst exponents and pre-factors (red lines in Figs. 9D–9E), while the roughest (i.e., Zone 4) is characterized by the higher scaling factors (orange lines in Figs. 9D–9E). Though erosive physico-chemical processes operate at smaller scales (i.e., at crystal scale), their impact upon larger scales of observation is evident in Figures 9D–9E. Indeed, one might have expected the power spectra to diverge mostly at their shorter wavelengths (i.e., at high spatial frequency). However, their power spectra diverge at spatial frequencies <9 mm^{-1} and are mostly overlapping at higher values. The sub-region from Zone 2 corresponds to a surface that is relatively smooth but marked by a deep groove (<1.2 mm) that is oblique to the slip vector, which relates to erosion by surface runoff. Its scaling factors fall within the range of the aforementioned end-members (Figs. 9D–9E). However, its power spectrum has values at larger
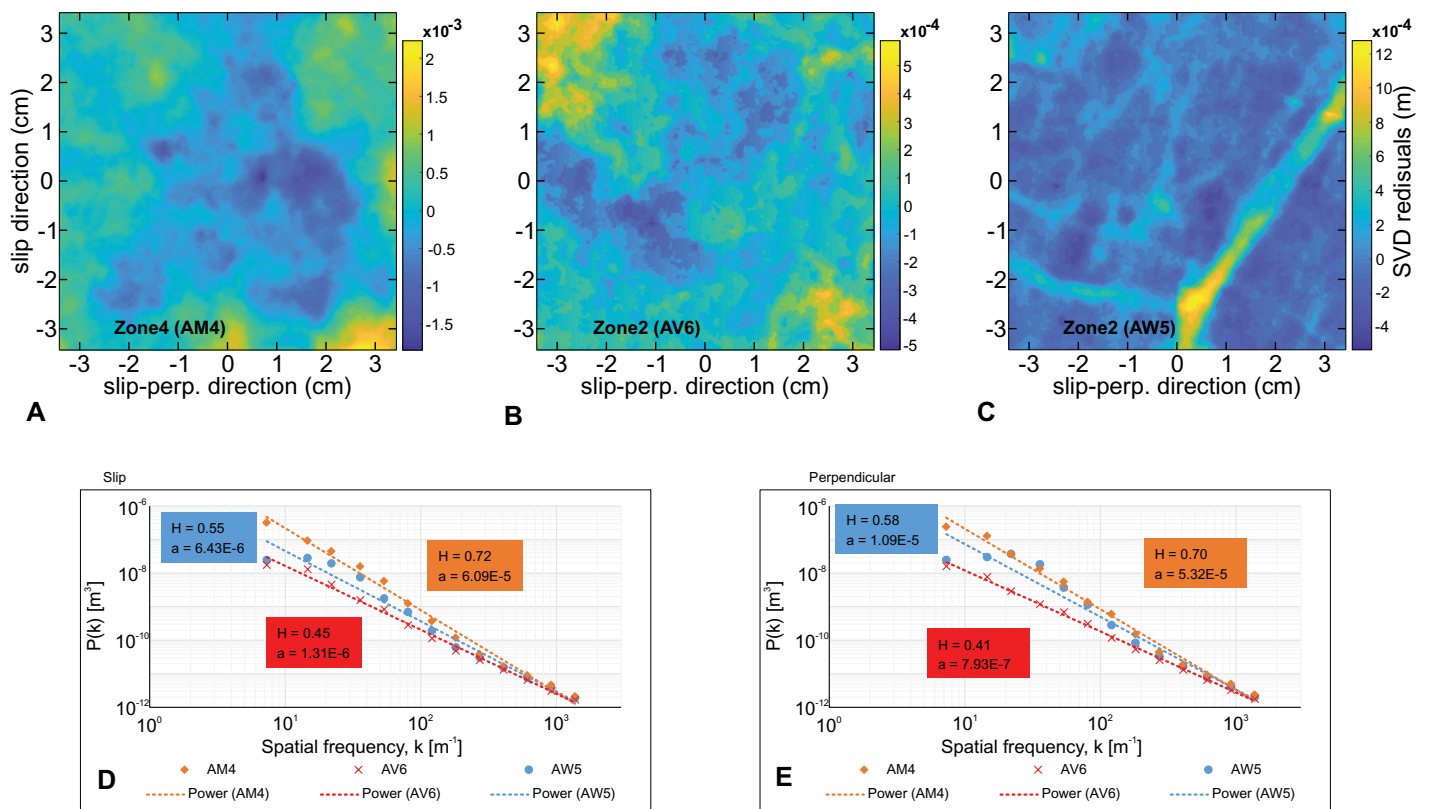
Figure 9. Overview shows results of the fast Fourier transform analysis over three representative fault surfaces: (A) a surface having a standard deviation representative of Zone 4; (B) a surface having the smallest standard deviation (belonging to Zone 2); (C) a surface having a standard deviation representative for Zone 2. Note that the scales are different. Power spectra of the three representative surfaces (D) along slip and (E) perpendicular to slip showing the dependence of asperities sizes with Hurst and pre-factor exponents. Rougher and more weathered surfaces have higher Hurst exponents and pre-factor values. SVD—singular value decomposition; perp.—perpendicular; H—Hurst exponent; a—pre-factor.

frequencies that deviate from the well-defined log-linear relationship. This deviation is due to the presence of the aforementioned erosional feature. In fact, the pre-factor of the power law (also known as topothesy) is a well-recognized parameter that is able to detect surface defects of engineering materials. Additional filtering in fault roughness analysis to exclude fractures from the analysis can thus be represented by the goodness of fit of a power spectrum density.

Normal faults expose new patches of the fault plane over every seismic cycle. Prior to being exposed to exogenous agents (e.g., weathering), it is reasonable to assume that in the absence of lithology variations a long-lived individual fault shows homogeneous roughness characteristics, particularly within short distances (<2 m). While reaching the surface, these patches are then subjected to time-dependent processes, especially weathering, that start degrading the seismically caused characteristics of the fault roughness. Accordingly, the method proposed here can be used to investigate the self-similarity of sub-areas along slip transects, allowing patches of the fault

with similar exposure time to be identified (e.g., He et al., 2016). In optimal cases, by recognizing different patches with the same degree of alteration, we hope to apply the method to estimate the amount of surface exposed during each recorded event; the derivative of the Hurst exponent will be used to mark the boundaries between adjacent exhumation events. This information can be crucial in seismic hazard assessment, since once the dimensional properties of a fault are constrained, the maximum expected magnitude is a function of the expected slip on a particular segment of the fault plane. However, discerning the timing and relative impact of subsurface processes, such as groundwater circulation and dissolution (i.e., within the vadose and phreatic zone) along the fault plane upon pristine (i.e., seismogenic) roughness is a non-trivial task. An additional factor limiting the identification of paleoseismic displacement on a given fault strand by means of exposition time estimators arises from the fact that not all fault denudation at surface can be assumed to be attributable to fault displacements.

CONCLUSIONS

In the study presented here we have used SfM-MVS photogrammetry to generate a highly detailed point cloud of an active carbonate transtensional fault exposed to weathering within the Northern Apennines of Central Italy. This was then used to quantify and compare the roughness of patches of the fault exposed to weathering over different timescales dictated by fault activity. Fault roughness was estimated by means of the standard deviation of the surfaces' residual distances from their plane of best fit and by measures of self-affinity. The latter can be estimated by interpolation of the PSD of the FFT. This latter approach provides an objective description of the roughness based on the distribution of asperities in the Fourier domain.

We have evidenced that even with active normal faults that are generally considered to represent the best available targets to study seismogenic roughness at macro to mesoscales, caution must be paid to the relative exposure time of the faulted outcrop analogue, since the effect

10

of weathering can have a profound impact upon the roughness characteristics of the fault plane. This is particularly pertinent to host lithologies that have a high degree of chemical susceptibility to weathering such as the faulted carbonates analyzed in this study. We suggest that fault roughness studies in outcrop should employ a piecewise approach to decipher the multiphase rupture and exposure history of the fault system and its resultant impact upon seismogenic fault plane roughness.

ACKNOWLEDGMENTS

REFERENCES CITED

Agosta, F., and Aydin, A., 2006, Architecture and deformation mechanism of a basin-bounding normal fault in Mesozoic platform carbonates, central Italy: Journal of Structural Geology, v. 28, p. 1445–1467, https://doi.org/10.1016/j.jsg.2006.04.006.

Andrews, D.J., 1980, A stochastic fault model: 1. Static case: Journal of Geophysical Research. Solid Earth, v. 85, B7, p. 3867–3877, https://doi.org/10.1029/JB085iB07p03867.

Bistacchi, A., Griffith, W.A., Smith, S.A.F., Di Toro, G., Jones, R.R., and Nielsen, S., 2011, Fault Roughness at Seismogenic Depths from LIDAR and Photogrammetric Analysis: Pure and Applied Geophysics, v. 168, no. 12, p. 2345–2363, https://doi.org/10.1007/s00024-011-0301-7.

Brace, W.F., and Byerlee, J.D., 1966, Stick-slip as a mechanism for earthquakes: Science, v. 153, p. 990–992, https://doi.org/10.1126/science.153.3739.990.

Brodsky, E.E., Gilchrist, J.J., Sagy, A., and Collettini, C., 2011, Faults smooth gradually as a function of slip: Earth and Planetary Science Letters, v. 302, p. 185–193, https://doi.org/10.1016/j.epsl.2010.12.010.

Brown, S.R., and Scholz, C.H., 1985, Broad bandwidth study of the topography of natural rock surfaces: Journal of Geophysical Research: Solid Earth, v. 90, https://doi.org/10.1029/JB090iB14p12575.

Candela, T., and Brodsky, E.E., 2016, The minimum scale of grooving on faults: Geology, v. 44, p. 603–606, https://doi.org/10.1130/G37934.1.

Candela, T., Renard, F., Bouchon, M., Brouste, A., Marsan, D., Schmittbuhl, J., and Voisin, C., 2009, Characterization of fault roughness at various scales: Implications of three-dimensional high resolution topography measurements: Pure and Applied Geophysics, v. 166, p. 1817–1851, https://doi.org/10.1007/s00024-009-0521-2.

Candela, T., Renard, F., Klinger, Y., Mair, K., Schmittbuhl, J., and Brodsky, E.E., 2012, Roughness of fault surfaces over nine decades of length scales: Journal of Geophysical Research: Solid Earth, v. 117, B08409, https://doi.org/10.1029/2011JB009041.

Chiaraluce, L., et al., 2017, The 2016 Central Italy seismic sequence: A first look at the mainshocks, aftershocks, and source models: Seismological Research Letters, v. 88, p. 757–771, https://doi.org/10.1785/0220160221.

Civico, R., Pucci, S., Villani, F., Pizzimenti, L., De Martini, P.M., and Nappi, R., 2018, Surface ruptures following the 30 October 2016 Mw 6.5 Norcia earthquake, central Italy: Journal of Maps, v. 14, p. 151–160, https://doi.org/10.1080/17445647.2018.1441756.

Collettini, C., Barchi, M.R., Chiaraluce, L., Mirabella, F., and Pucci, S., 2003, The Gubbio fault: Can different methods give pictures of the same object?: Journal of Geodynamics, v. 36, p. 51–66, https://doi.org/10.1016/S0264-3707(03)00038-3.

Corradetti, A., McCaffrey, K.J.W., De Paola, N., and Tavani, S., 2017, Evaluating roughness scaling properties of natural active fault surfaces by means of multi-view photogrammetry: Tectonophysics, v. 717, p. 599–606, https://doi.org/10.1016/j.tecto.2017.08.023.

Corradetti, A., Tavani, S., Parente, M., Iannace, A., Vinci, F., Pirmez, C., Torrieri, S., Giorgioni, M., Pignalosa, A., and Mazzoli, S., 2018, Distribution and arrest of vertical through-going joints in a seismic-scale carbonate platform exposure (Sorrento peninsula, Italy): Insights from integrating field survey and digital outcrop model: Journal of Structural Geology, v. 108, p. 121–136, https://doi.org/10.1016/j.jsg.2017.09.009.

De Paola, N., Holdsworth, R.E., Viti, C., Collettini, C., and Bullock, R., 2015, Can grain size sensitive flow lubricate faults during the initial stages of earthquake propagation?: Earth and Planetary Science Letters, v. 431, p. 48–58, https://doi.org/10.1016/j.epsl.2015.09.002.

Doblas, M., 1998, Slickenside kinematic indicators: Tectonophysics, v. 295, p. 187–197, https://doi.org/10.1016/S0040-1951(98)00120-6.

Fernández, O., 2005, Obtaining a best fitting plane through 3D georeferenced data: Journal of Structural Geology, v. 27, p. 855–858, https://doi.org/10.1016/j.jsg.2004.12.004.

Galli, P., and Galadini, F., 1999, Seismotectonic framework of the 1997–1998 Umbria-Marche (Central Italy) earthquakes: Seismological Research Letters, v. 70, p. 417–427, https://doi.org/10.1785/gssrl.70.4.417.

Galli, P., Galderisi, A., Peronace, E., Giaccio, B., Hajdas, I., Messina, P., Pileggi, D., and Polpetta, F., 2019, The awakening of the dormant Mount Vettore Fault (2016 Central Italy earthquake, Mw 6.6): Paleoseismic clues on its millennial silences: Tectonics, v. 38, p. 687–705, https://doi.org/10.1029/2018TC005326.

Giuffrida, A., Agosta, F., Rustichelli, A., Panza, E., La Bruna, V., Eriksson, M., Torrieri, S., and Giorgioni, M., 2020, Fracture stratigraphy and DFN modelling of tight carbonates, the case study of the Lower Cretaceous carbonates exposed at the Monte Alpi (Basilicata, Italy): Marine and Petroleum Geology, v. 112, no. 104045, https://doi.org/10.1016/j.marpetgeo.2019.104045.

Goldberg, R., Siman-Tov, S., and Emmanuel, S., 2016, Weathering resistance of carbonate fault mirrors promotes rupture localization: Geophysical Research Letters, v. 43, p. 3105–3111, https://doi.org/10.1002/2016GL067788.

Golub, G.H., and Reinsch, C., 1971, Singular Value Decomposition and Least Squares Solutions, in Linear Algebra: Berlin, Springer, p. 134–151, https://doi.org/10.1007/978-3-662-39778-7_10.

Goodman, R.E., and Sundaram, P.N., 1978, Fault and system stiffnesses and stick-slip phenomena: PAGEOPH, v. 116, p. 873–887, https://doi.org/10.1007/BF00876543.

He, H., Wei, Z., and Densmore, A., 2016, Quantitative morphology of bedrock fault surfaces and identification of paleo-earthquakes: Tectonophysics, v. 693, p. 22–31, https://doi.org/10.1016/j.tecto.2016.09.032.

James, M.R., and Robson, S., 2012, Straightforward reconstruction of 3D surfaces and topography with a camera: Accuracy and geoscience application: Journal of Geophysical Research: Earth Surface, v. 117, no. F03017, https://doi.org/10.1029/2011JF002289.

Jones, R.R., Pearce, M.A., Jacquemyn, C., and Watson, F.E., 2016, Robust best-fit planes from geospatial data: Geosphere, v. 12, p. 196–202, https://doi.org/10.1130/GES01247.1.

Mandelbrot, B.B., 1985, Self-affine fractals and fractal dimension: Physica Scripta, v. 32, p. 257–260, https://doi.org/10.1088/0031-8949/32/4/001.

Mazzoli, S., Pierantoni, P.P., Borraccini, F., Paltrinieri, W., and Deiana, G., 2005, Geometry, segmentation pattern and displacement variations along a major Apennine thrust zone, central Italy: Journal of Structural Geology, v. 27, p. 1940–1953, https://doi.org/10.1016/j.jsg.2005.06.002.

Mills, G., and Fotopoulos, G., 2013, On the estimation of geological surface roughness from terrestrial laser scanner point clouds: Geosphere, v. 9, p. 1410–1416, https://doi.org/10.1130/GES00918.1.

Mora, P., and Place, D., 1999, The weakness of earthquake faults: Geophysical Research Letters, v. 26, p. 123–126, https://doi.org/10.1029/1998GL900231.

NASA/METI/AIST/Japan Spacesystems and U.S./Japan Aster Science Team, 2019, ASTER Global Digital Elevation Model V003: distributed by NASA EOS-DIS Land Processes DAAC, https://doi.org/10.5067/ASTER/ASTGTM.003.

Okamoto, K.K., Brodsky, E.E., Thom, C.A., Smeraglia, L., and Billi, A., 2019, The Minimum Scale of Grooving on a Recently Ruptured Limestone Fault: Geophysical Research Letters, v. 46, p. 11878–11885, https://doi.org/10.1029/2019GL084889.

Okubo, P.G., and Dieterich, J.H., 1984, Effects of physical fault properties on frictional instabilities produced on simulated faults: Journal of Geophysical Research: Solid Earth, v. 89, p. 5817–5827, https://doi.org/10.1029/JB089iB07p05817.

Olkowicz, M., Dabrowski, M., and Pluymakers, A., 2019, Focus stacking photogrammetry for micro-scale roughness reconstruction: A methodological study: The Photogrammetric Record, v. 34, p. 11–35, https://doi.org/10.1111/phor.12270.

Pierantoni, P.P., Deiana, G., and Galdenzi, S., 2013, Stratigraphic and structural features of the Sibillini Mountains (Umbria-Marche Apennines, Italy): Italian Journal of Geosciences, v. 132, p. 497–520, https://doi.org/10.3301/IJG.2013.08.

Pitts, A.D., Casciano, C.I., Patacci, M., Longhitano, S.G., Di Celma, C., and McCaffrey, W.D., 2017, Integrating traditional field methods with emerging digital techniques for enhanced outcrop analysis of deep water channel-fill deposits: Marine and Petroleum Geology, v. 87, p. 2–13, https://doi.org/10.1016/j.marpetgeo.2017.05.001.

Pluymakers, A., and Røyne, A., 2017, Nanograin formation and reaction-induced fracturing due to decarbonation: Implications for the microstructures of fault mirrors: Earth and Planetary Science Letters, v. 476, p. 59–68, https://doi.org/10.1016/j.epsl.2017.08.001.

Pluymakers, A., Kobchenko, M., and Renard, F., 2017, How microfracture roughness can be used to distinguish between exhumed cracks and in-situ flow paths in shales: Journal of Structural Geology, v. 94, p. 87–97, https://doi.org/10.1016/j.jsg.2016.11.005.

Porreca, M., Fabbrizzi, A., Azzaro, S., Pucci, S., Del Rio, L., Pierantoni, P.P., Giorgetti, C., Roberts, G., and Barchi, M.R., 2020, 3D geological reconstruction of the M. Vettore seismogenic fault system (Central Apennines, Italy): Cross-cutting relationship with the M. Sibillini thrust: Journal of Structural Geology, v. 131, no. 103938, https://doi.org/10.1016/j.jsg.2019.103938.

Power, W.L., and Tullis, T.E., 1991, Euclidean and fractal models for the description of rock surface roughness: Journal of Geophysical Research: Solid Earth, v. 96, p. 415, https://doi.org/10.1029/90JB02107.

Power, W.L., Tullis, T.E., Brown, S.R., Boitnott, G.N., and Scholz, C.H., 1987, Roughness of natural fault surfaces: Geophysical Research Letters, v. 14, p. 29–32, https://doi.org/10.1029/GL014i001p00029.

Renard, F., Candela, T., and Bouchaud, E., 2013, Constant dimensionality of fault roughness from the scale of micro-fractures to the scale of continents: Geophysical Research Letters, v. 40, p. 83–87, https://doi.org/10.1029/2012GL054143.

Sagy, A., Brodsky, E.E., and Axen, G.J., 2007, Evolution of fault-surface roughness with slip: Geology, v. 35, p. 283, https://doi.org/10.1130/G23235A.1.

Schmittbuhl, J., Gentier, S., and Roux, S., 1993, Field measurements of the roughness of fault surfaces: Geophysical Research Letters, v. 20, p. 639–641, https://doi.org/10.1029/93GL00170.

Schuster, A., 1898, On the investigation of hidden periodicities with application to a supposed 26 day period of meteorological phenomena: Journal of Geophysical Research, v. 3, p. 13, https://doi.org/10.1029/TM003i001p00013.

Seers, T.D., and Hodgetts, D., 2016, Probabilistic constraints on structural lineament best fit plane precision obtained through numerical analysis: Journal of Structural Geology, v. 82, p. 37–47, https://doi.org/10.1016/j.jsg.2015.11.004.

Siman-Tov, S., Aharonov, E., Sagy, A., and Emmanuel, S., 2013, Nanograins form carbonate fault mirrors:

Geology, v. 41, p. 703–706, https://doi.org/10.1130/G34087.1.

Smeraglia, L., Billi, A., Carminati, E., Cavallo, A., and Doglioni, C., 2017, Field- to nano-scale evidence for weakening mechanisms along the fault of the 2016 Amatrice and Norcia earthquakes, Italy: Tectonophysics, v. 712–713, p. 156–169, https://doi.org/10.1016/j.tecto.2017.05.014.

Tal, Y., Hager, B.H., and Ampuero, J.P., 2018, The Effects of Fault Roughness on the Earthquake Nucleation Process: Journal of Geophysical Research. Solid Earth, v. 123, no. 1, p. 437–456, https://doi.org/10.1002/2017JB014746.

Telling, J., Lyda, A., Hartzell, P., and Glennie, C., 2017, Review of Earth science research using terrestrial laser scanning: Earth-Science Reviews, v. 169, p. 35–68, https://doi.org/10.1016/j.earscirev.2017.04.007.

Thompson, M.E., and Brown, S.R., 1991, The effect of anisotropic surface roughness on flow and transport in fractures: Journal of Geophysical Research:

Solid Earth, v. 96, p. 21923–21932, https://doi.org/10.1029/91JB02252.

Tondi, E., and Cello, G., 2003, Spatiotemporal evolution of the Central Apennines fault system (Italy): Journal of Geodynamics, v. 36, p. 113–128, https://doi.org/10.1016/S0264-3707(03)00043-7.

Tullis, T.E., 1988, Rock friction constitutive behavior from laboratory experiments and its implications for an earthquake prediction field monitoring program: PAGEOPH, v. 126, p. 555–588, https://doi.org/10.1007/BF00879010.

Villani, F., Pucci, S., Civico, R., De Martini, P.M., Cinti, F.R., and Pantosti, D., 2018, Surface faulting of the 30 October 2016 Mw 6.5 Central Italy earthquake: Detailed analysis of a complex coseismic rupture: Tectonics, v. 37, p. 3378–3410, https://doi.org/10.1029/2018TC005175.

Wei, Z., He, H., and Shi, F., 2013, Weathering history of an exposed bedrock fault surface interpreted from its topography: Journal of Structural Geology, v. 56, p. 34–44, https://doi.org/10.1016/j.jsg.2013.08.008.

Wiatr, T., Papanikolaou, I., Fernández-Steeger, T., and Reicherter, K., 2015, Reprint of: Bedrock fault scarp history: Insight from t-LiDAR backscatter behaviour and analysis of structure changes: Geomorphology, v. 237, p. 119–129, https://doi.org/10.1016/j.geomorph.2015.02.019.

Zambrano, M., Pitts, A.D., Salama, A., Volatili, T., Giorgioni, M., and Tondi, E., 2019, Analysis of fracture roughness control on permeability using SfM and fluid flow simulations: Implications for carbonate reservoir characterization: Geofluids, v. 2019, p. 1–19, https://doi.org/10.1155/2019/4132386.